



Deposited via The University of Leeds.

White Rose Research Online URL for this paper:

<https://eprints.whiterose.ac.uk/id/eprint/182763/>

Version: Accepted Version

Article:

Liu, Q, Yang, S, Shen, L et al. (2020) The effect of hydrogen concentration on the fracture surface of medium Mn steels. *Engineering Failure Analysis*, 108. 104263. ISSN: 1350-6307

<https://doi.org/10.1016/j.engfailanal.2019.104263>

© 2019, Elsevier. This manuscript version is made available under the CC-BY-NC-ND 4.0 license <http://creativecommons.org/licenses/by-nc-nd/4.0/>.

Reuse

This article is distributed under the terms of the Creative Commons Attribution-NonCommercial-NoDerivs (CC BY-NC-ND) licence. This licence only allows you to download this work and share it with others as long as you credit the authors, but you can't change the article in any way or use it commercially. More information and the full terms of the licence here: <https://creativecommons.org/licenses/>

Takedown

If you consider content in White Rose Research Online to be in breach of UK law, please notify us by emailing eprints@whiterose.ac.uk including the URL of the record and the reason for the withdrawal request.

1 parts, determined by the stability and content of RA. Slow strain rate tensile tests with
2 hydrogen charging were performed to investigate the behaviour of hydrogen diffusion and the
3 mechanism of hydrogen embrittlement (HE). After the tests, the hydrogen content was
4 measured and the fracture surface was observed and analysed. The phenomenon of HE in
5 steels has been mainly explained based on the mechanisms of hydrogen-enhanced localised
6 plasticity (HELP), hydrogen-enhanced decohesion (HEDE), and hydrogen assisted micro
7 ovoid coalescence (HDMC). Due to the existence of hydrogen, fracture morphology changes
8 from ductile mode to brittle mode. It was also found that under the same strain rate, tensile
9 strength and elongation decrease gradually as hydrogen concentration increases, resulting in
10 final failure.

11 **Key words:**

12 **Medium Mn steel; Hydrogen embrittlement; Fracture morphology**
13

14 **1. Introduction**

15 Nowadays, in the automobile industry, weight reduction, energy saving and safety
16 improvement are urgently required. Over the past decades, automobile manufacturers have
17 mainly considered the cost, formability and corrosion resistance of advanced high strength
18 steels (AHSSs) with typically multiphase microstructures. Tensile strength and total
19 elongation (PSE) were called in to value the mechanical properties of AHSSs. Generally, dual
20 phase (DP), martensitic (MART) and transformation-induced plasticity (TRIP) steels are
21 referred to as the first generation AHSSs with a PSE of 10~20GPa•%, while
22 twinning-induced plasticity (TWIP) steels, austenitic steels and lightweight steels with
23 induced plasticity (L-IP) are referred to as the second generation AHSSs with a PSE of
24 50~70GPa•%. Compared with the first generation AHSSs, higher manufacturing costs and
25 alloying levels severely limited the use of second generation AHSSs. Thus, a third generation
26 AHSSs, with a better strength–ductility combination and lower cost, are urgently needed.

1 Miller developed the medium Mn steel with 4~10wt% Mn [1]. Mn [1, 2] promotes austenite
2 formation and increases the volume fraction of retained austenite in medium Mn steel at room
3 temperature. Thus, the microstructure of medium Mn steel has a dual phase of ferrite and
4 austenite (typically 20~40 vol%). Due to its good combination of strength and elongation,
5 many scientists have investigated the deformation mechanism and mechanical properties of
6 medium Mn steel [3]. The areas of focus were the tensile behaviours and deformation [3],
7 intercritical annealing conditions [4, 5], fracture characterisation [6], alloying elements [7, 8],
8 the influence of the initial microstructure of α' martensite before intercritical annealing [9-11]
9 and the warm ductility [4] of medium Mn steel.

10 Hydrogen in high strength steels and alloys has a most common effect, hydrogen
11 embrittlement (HE) [12-14]. Generally, the higher strength materials are more susceptible to
12 HE [15, 16]. It is defined as the process by which strength and ductility of a material can
13 reduced significantly by introduction of hydrogen atom when working on hydrogen
14 environment [16]. Factors which are responsible for susceptibility of materials for HE can be
15 concluded as the synergistic action of materials (nature and surface condition), stress
16 (residual stress and applied strain rate) and environment (concentration of hydrogen,
17 temperature, pressure and solution react with metals) [15, 17, 18]. Liu [19] has explained
18 hydrogen influence on DP, QP and TWIP steels. Depover [20] has investigated the effect of
19 hydrogen charging on the mechanical properties of TRIP, Ferrite Bainitic (FB), DP and High
20 Strength Low Alloy (HSLA) steels, and Han [21] has examined hydrogen embrittlement
21 under intercritically annealed conditions, while hydrogen redistribution under stress-induced
22 diffusion was investigated in structural steel [22].

23 Medium Mn steel, with various advantages such as excellent strength and ductility, is easily
24 vulnerable to hydrogen embrittlement (HE) [23]. Koyama[24] has reported that the HE
25 susceptibility of medium Mn steels is particularly sensitive to their chemical composition and
26 alloying elements, which affect the stacking fault energy (SFE), austenite phase stability and
27 associated hydrogen segregation on the phase, grain, and twin boundaries. These factors
28 affect micro-stress concentrations and the local diffusible hydrogen content, which acts on the
29 hydrogen-enhanced localised plasticity (HELP) effect [25], on hydrogen-enhanced

1 decohesion (HEDE) [26], on adsorption-induced dislocation emission (AIDE) [27], on
2 hydrogen assisted micro void coalescence (HDMC) [16], as well as on hydrogen-enhanced
3 and strain-induced vacancies (HESIV) formation[28, 29]. Sometime combination of these
4 mechanisms is responsible for degradation and embrittlement of material.

5 Some researchers studied that the influence of hydrogen content on the tensile properties and
6 fracture modes could be classified into two cases in the high Mn steel [30]. The samples with
7 low diffusible hydrogen content (e.g. 0.33 wt.ppm) showed a ductile fracture while the
8 samples with relatively high diffusible hydrogen content (e.g.1.24 wt.ppm) showed an
9 intergranular fracture. Due to the effect of hydrogen, material became brittle and crack
10 growth happened due to dislocation emission or microvoid coalescence (MVC) [16]. From
11 this view, combination of both dislocation emission and MVC may be responsible for crack
12 growth and ultimately fracture happened in material.

13 The interaction of hydrogen content, applied stress and fracture morphology **for medium Mn**
14 **steels**, however, are rarely reported in the literatures. The study of fracture mode is required
15 for knowledge of how the crack can grow in the material and how the fracture can be
16 influenced due to the effect of hydrogen. Therefore, in this paper, we investigated
17 systematically the role of hydrogen in influencing the fracture surface and mechanical
18 properties of medium Mn steels.

19 **2. Experiment Materials and Methods**

20 **2.1 Materials**

21 The medium Mn steels (MMSs) thin plates were supplied by Baoshan Iron & Steel Co., Ltd.
22 In this study, the mechanical properties and hydrogen-induced cracking of medium Mn steels
23 were investigated. The main differences between the three kinds of manganese steel are the
24 Mn content and heat treatment process [31].

25 The heat treatment detail involved hot-rolled, intercritically batch-annealed and cold-rolled

1 treatment. After steelmaking, the slabs were heated to 1473 K for two hours and hot-rolled in
 2 a temperature of 1153 K. Intercritical batch annealing was conducted at 893 K for 12 hours.
 3 The thickness for hot-rolled sheets was 2.8mm, consisting of austenite and ferrite. Then, the
 4 sheets were pickled and cold-rolled to a thickness of 1.4mm and the thickness conduction
 5 was 50pct. The cold-rolled medium Mn steel sheets were heated to 893 K and held for three
 6 minutes and 12 hours. The annealing time is relevant to the continuous annealing and
 7 batch-annealing processes respectively.

8 Table 1 lists the chemical composition of the material. The samples prepared in these two
 9 annealing conditions are designated as “M7B”, “M7C” and “M10B” respectively, ‘M’
 10 referring to Mn, ‘7’ or ‘10’ meaning the content of Mn, ‘B’ denoting batch annealing and ‘C’
 11 continuous annealing. Transmission electron microscope (TEM) and scanning electron
 12 microscopy (SEM) were used to observe the microstructure and fracture morphology.

13 **Table 1 Chemical composition in wt. % of MMSs**

Material/element	C	Si	Mn	Cr	Al	Fe
M7B	0.14	0.23	7.16	0.077	0.055	balance
M7C	0.14	0.23	7.14	0.082	0.056	balance
M10B	0.15	0.17	10.40	0.073	1.49	balance

14

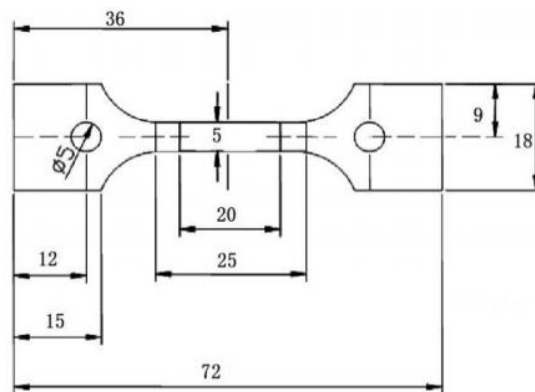
15 **2.2 Hydrogen permeation tests**

16 A double electrolytic cell for hydrogen permeation test was used in this study to investigate
 17 the diffusion behaviour of hydrogen in MMSs. In this work, the sample shape was designed
 18 like a coin with a diameter of 20mm. Prior to the permeation test, the specimen was ground
 19 with SiC paper up to 5,000 grits and, then, ultrasonically cleansed in acetone. In order to
 20 avoid the corrosion or passivation of the sample in the solution, nickel coating is usually
 21 required on the surface of the sample. The Ni electroplating solution is
 22 250gNiSO₄-7H₂O+45gNiCl₂-6H₂O+40gH₃BO₄/L with a current density of 10mA/cm² for 60s.
 23 The hydrogen-charging solution in the charging side was 0.2molL⁻¹ NaOH + 0.22 gL⁻¹
 24 thiourea (H₂NCSNH₂) with 5mAcm⁻² charging current density at room temperature,

1 approximately 25°C, while the solution in the escaping side was 0.2mol L⁻¹ NaOH [22].

2 **2.3 Slow strain rate tensile tests**

3 Slow strain rate tensile tests (SSRT) have gradually become a classical method for studying
4 susceptibility to hydrogen embrittlement (HE), which can be determined by measuring the
5 fracture stress drop, the reduction of the area and the elongation of the material before and
6 after hydrogen charging [22]. The specimen of MMSs used in this study was designed
7 according to ASTM E8, shown in Figure 1. The tensile specimens were 1.5mm thick, and
8 their surfaces were wet-ground with SiC paper up to 2,000 grit, and then ultrasonically
9 cleansed in acetone and ethanol. The strain was recorded from the cross-head displacement.
10 The test strain rate was 1×10⁻⁶ s⁻¹.



12 **Fig. 1 Schematic diagram of MMSs tensile specimen (dimensions in mm) [32]**

13
14
15 For three kinds of MMSs, electrochemical hydrogen charging was implemented in
16 0.2mol•L⁻¹ sulphuric acid (H₂SO₄) and 0.22 g•L⁻¹ thiourea solution with a current density of
17 1mA•cm⁻². The specimen was the cathode and the Pt wire was the anode. According to the
18 coefficient of hydrogen diffusion, hydrogen charging time is three hours, eight hours and 24
19 hours respectively, and hydrogen charging current density is 1mA/cm². Only the gauge part
20 of the sample was charged, because other parts were sealed by silica gel. Fracture
21 morphology was observed by a Qyanta FEG 450 scanning electron microscope (SEM), and
22 hydrogen concentration was measured by G4 Phoenix DH at 800 Celsius for 20 min.

1 Diffusible Hydrogen Analyser G4 PHOENIX, utilising the carrier gas hot extraction method,
2 enables the rapid and automatic determination of diffusible hydrogen in a wide variety of
3 matrices. The analyser is equipped with a rapid heating (and cooling) infrared-heated
4 clamshell furnace (up to 900 Celsius). The quartz tube diameter of 30 mm enables the
5 analysis of large samples like steel sheet strips, as well as weld coupons according to ISO
6 3690 and AWS A4.3. 800 Celsius was set as the analysis temperature because it can make all
7 hydrogen in the sample escape. Analysis time depended on sample material, weight and
8 analysis temperature, typically 15–20 min.

9 **3. Results and discussion**

10 **3.1 Microstructure and tensile behaviour**

11 Fig. 2 presents TEM images of test steels. Due to the ultrafine grained size of test steel, we
12 use the TEM to observe the grain and phase structure more clearly. As is known, MMSs have
13 a dual phase of ferrite and retained austenite. The convex and concave parts of MMSs
14 represent ferrite and retained austenite respectively. M7B is uniformly distributed with
15 globular-shaped ferrite and retained austenite, with a grain size of about 1–3 μm . The
16 microstructure of M7C is mainly distributed with lath-shaped austenite and ferrite, which is
17 mainly due to incomplete annealing. Lengthy batch annealing leads to the recrystallisation of
18 martensite. When it reverts to austenite, long-strip austenite can be combined into block
19 austenite. Continuous annealing for 1–3 minutes can promote the transformation of
20 martensite to austenite, but its microstructure still retains the characteristics of lath martensite.

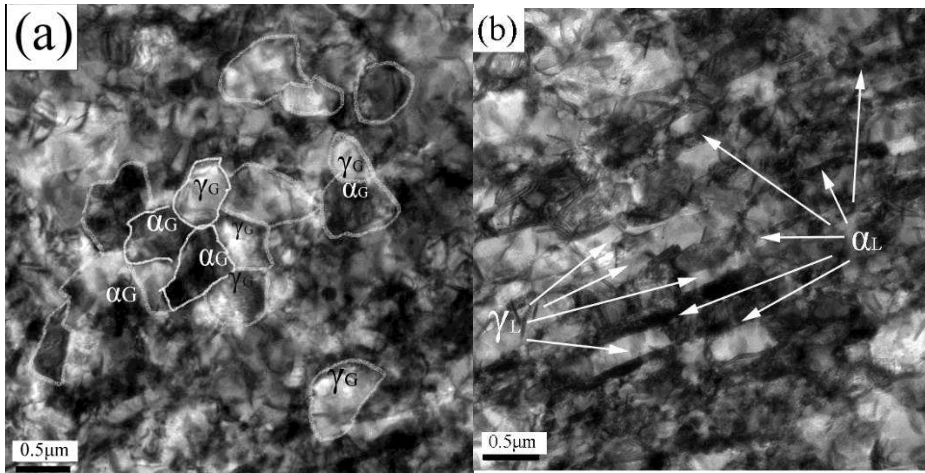


**Fig. 2 TEM micrographs of (a)M7B and(b) M7C
 α_L and γ_L are lath-shaped ferrite and retained austenite, α_G and γ_G are
globular-shaped ferrite and retained austenite.**

The engineering stress-strain curve of the MMSs after different annealing processes was shown in Fig. 3. The strain rate in air is $1 \times 10^{-4} \text{s}^{-1}$. The steels exhibit an excellent combination of high strength and ductility; M7B for example measures 745MPa for yield stress, 1133MPa for tensile strength and about 31.3% of total elongation. The product of tensile strength to ductility for M7B is about 35.5 GPa%, for M7C 34.3 GPa% and for M10B 56.1GPa%, listed in Table 2.

Table 2 Mechanical properties of three kinds of MMSs

Steel	Yield stress/MPa	Tensile strength/MPa	Ductility /%	The product of TS and ductility/GPa•%
M7B	745	1133	31.3%	35.5
M7C	1113	1130	30.4%	34.3
M10B	794	1403	40.0%	56.1

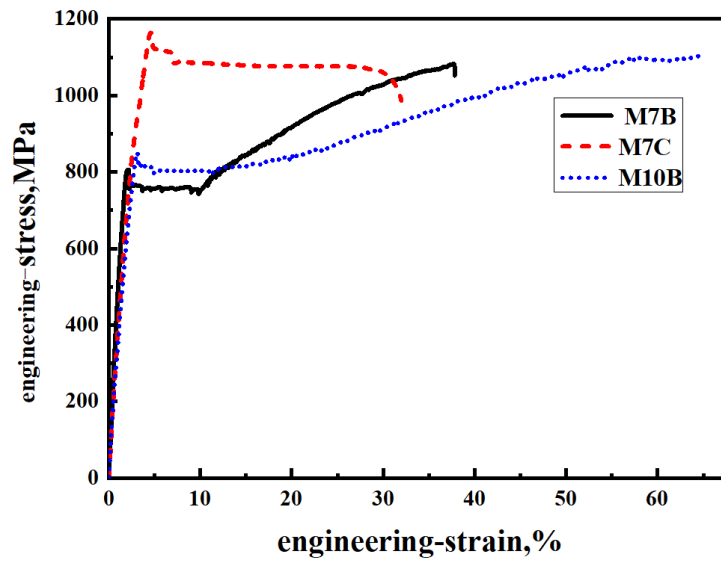
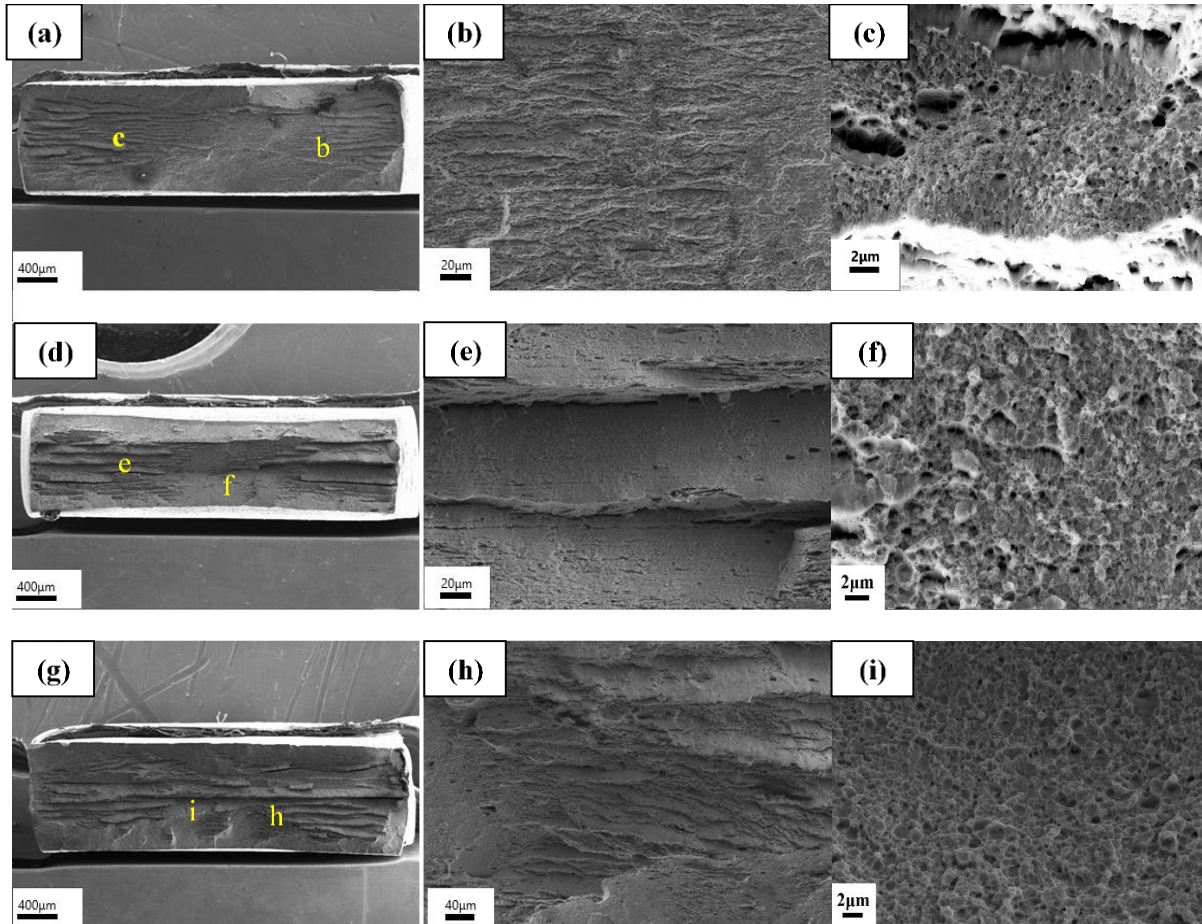


Fig. 3 Engineering stress-strain curves of MMSs

For M7B and M10B, the tensile curve consists of three parts: (1) the elastic strain stage; (2) the stress dropping and yield stage, showing plastic instability; (3) the work hardening stage, whereby stress increases alongside strain. The reasons are as follows: the Cottrell atmosphere leads to stress concentration in the stretching process, and the deformation is not uniform in order to form the yield platform. The stress relaxation mechanism of austenite leads to martensite transformation and produces stress relaxation during the strain process. The stress of M7C reaches a higher level at lower strain, its yield strength is much higher than M7B and M10B, and then the stress is reduced, showing no obvious hardening. This is due to the poor stability of austenite in M7C, which has been transformed into martensite at lower strain conditions in M7C.

Fig. 4 shows the fracture surface of the specimen after SSRT in air. Without necking in the fracture, it shows that uniform deformation mainly occurs within the gauge part. In the MMSs fracture, there are many parallel tear edges, delamination and the distribution of some holes[33]. Some researchers reckoned that during the tensile process delamination was caused by the initiation of micro-cracks at non-metallic inclusions in the ferrite belt, where the micro-cracks combined together and finally forming delamination at the fracture [34]. Others believed that the delamination fracture appeared at half thickness of the cross section, where stress exceeded yield strength to accelerate the occurrence of the crack source in the

1 half thickness of the cross section of the specimen during tension test [35]. It is shown that
2 metastable austenite reduces stress concentration of the interface by the phase transformation
3 during the tensile test [36]. The ferrite alleviates stress concentration at the crack tip to delay
4 crack propagation by deformation.



5
6 **Fig. 4 SEM observation of fracture surfaces (a) (b) (c) for M7B; (d) (e) (f) for M7C; (g)**
7 **(h) (i) for M10B**

8 **3.2 Stability of retained austenite**

9 It has been mentioned that work hardening behaviour is closely related to the martensitic
10 transformation of retained austenite during the tensile process in MMSs. Thus, it is necessary
11 to study the mechanism of phase transformation and the stability of retained austenite during
12 uniaxial tension. The volume fraction of retained austenite (RA) under different plastic strain
13 was measured. Austenite was characterised by an FCC structure and ferrite by a BCC
14 structure [21]. X-ray diffraction can be used to determine the volume fraction of RA in

1 MMSs. Fig. 5 shows the XRD spectra of MMSs specimens before the tensile test. Based on
 2 the integrated intensities of $(200)_\gamma$, $(220)_\gamma$, $(331)_\gamma$, $(211)_\alpha$ and $(200)_\alpha$ diffraction peaks, the
 3 calculation of the volume fraction of retained austenite (RA) was performed using the
 4 following Eq. (1):

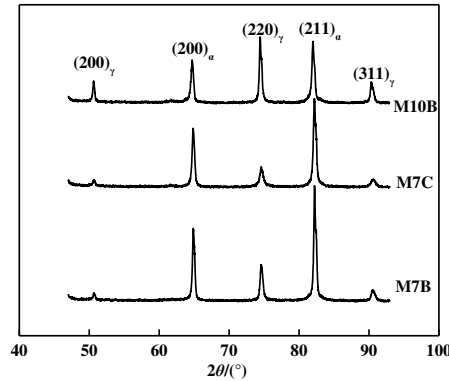
$$V_\gamma = 1.4I_\gamma / (I_\alpha + 1.4I_\gamma) \quad (1)$$

6 where I_α is the mean integrated intensity of two ferrite diffraction peaks, $(211)_\alpha$ and $(200)_\alpha$; I_γ
 7 is the mean integrated intensity of the three austenite diffraction peaks, $(200)_\gamma$, $(220)_\gamma$ and
 8 $(331)_\gamma$. Fig. 6 shows the volume fraction of RA for those samples with different pre-strain of
 9 0 (as received), 5, 10 and 15%.

10 The stability of RA is expressed in terms of the law of martensitic transformation based
 11 on the OC model [37], shown as Eq.(2):

$$K = -\frac{\ln(f_r / f_{r0})}{\varepsilon} \quad (2)$$

13 where f_{r0} is the volume fraction of RA before strain and f_r is the volume fraction of RA after
 14 strain of ε . K is the stability coefficient of RA. The smaller the K value is, the more stable the
 15 RA.



16
 17 **Fig. 5 X-Ray diffraction profiles of MMSs**

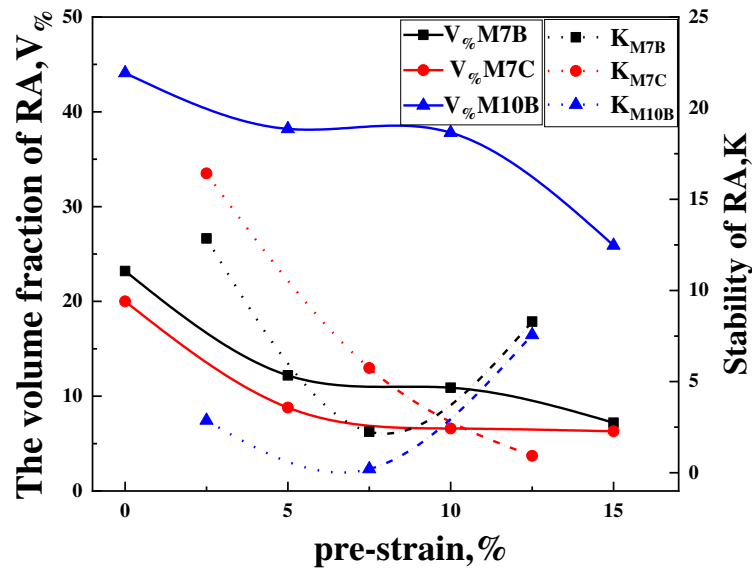


Fig. 6 The volume fraction and stability of RA in MMSs

The solid line and dotted line refer to the volume fraction and stability of RA, respectively.

According to the analysis of the stress strain curve in Fig. 3, pre-strain of 0-0.05 corresponds to the elastic stage and the initial yielding stage, when a large number of RA with poor stability induces martensitic transformation in M7B and M7C. Pre-strain of 0.05–0.10 corresponds to the yielding platform, when the deformation mainly depends on the Lüders strain in the ferrite matrix. M7B and M10B induce obvious work hardening, and martensitic transformation occurs to reduce local stress concentration as pre-strain continues to increase, with the stability coefficient of RA increasing synchronously. Due to the poor stability of austenite for M7C, no obvious work hardening was observed.

The volume fraction and stability of RA under different strain conditions was analysed and calculated by XRD. The stress-strain curve of MMSs can be divided into three stages, which depends on the content and stability of RA. After a short period of continuous annealing treatment, the stability of austenite in M7C is poor, while it has obviously transformed at the beginning of strain. Therefore, no obvious work hardening was observed on the nominal stress – nominal strain curves. The stability of RA in M7B and M10B is relatively high.

3.3 Hydrogen permeation

Fig. 7 is the hydrogen permeation curve of MMSs at room temperature. As can be seen from the curve, the anode current will rise with the hydrogen charging process until a steady state is reached. $t_{0.63}$ was the corresponding time of $I_a/I_\infty=0.63$ to calculate the diffusion coefficient using the following formula:

$$D = \frac{L^2}{6t_{0.63}} \quad (3)$$

The hydrogen diffusion coefficient of MMSs was shown in Table 3. It can be seen that the apparent hydrogen diffusion coefficient of M7B and M7C is similar, but M10B is lower than M7B and M7C by one order of magnitude.

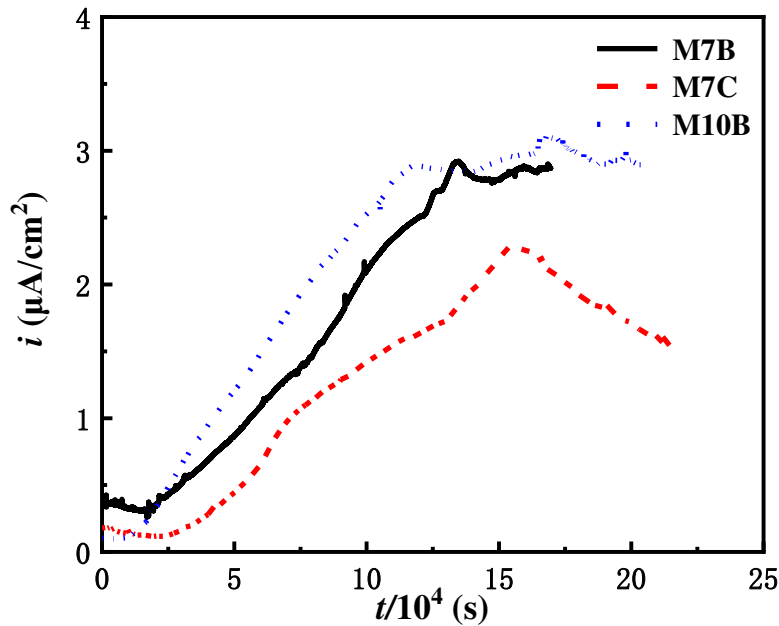


Fig. 7 Hydrogen permeation curves for MMSs

According to microstructure observation and XRD analysis, the main reason for the different hydrogen diffusivity of MMSs is the different volume fraction of austenite. The micrograph of MMSs is characterised by a dual phase consisting of ferrite and austenite. The rate of hydrogen diffusion in ferrite is 4–5 orders of magnitude higher than that in austenite, while hydrogen solubility in austenite is 2–3 orders of magnitude higher than that of ferrite.

1 Austenite, as a barrier to hydrogen diffusion, leads to a tortuous diffusion path [38], which
2 reduces the diffusion rate of hydrogen in MMSs. The volume fraction of austenite in M10B is
3 higher than that of M7B and M7C.

4 **Table 3 Details of D and $t_{0.63}$ for MMSs**

Material	$t_{0.63}(s)$	$L(cm)$	$D(cm^2/s)$
M7B	88658	0.128	3.08×10^{-8}
M7C	101538	0.132	2.86×10^{-8}
M10B	73167	0.044	0.441×10^{-8}

5
6 **3.4 Slow strain rate test with hydrogen charging**

7 Fig. 8 shows the nominal stress – nominal strain curves of MMSs under various hydrogen
8 pre-charged condition. The strain is not measured with a local extensometer but from the
9 cross-head displacement [22]. Therefore, the slope of the linear part of the curve does not
10 correspond to the elastic modulus of the steel. The elongation and fracture stress decreased
11 with the increasing time of hydrogen charge from 3 hours to 24 hours. Although the hydrogen
12 charging did not affect the work hardening behaviour much even when the hydrogen
13 embrittlement occurred [30]. For M7B and M10B, due to the presence of a yielding plateau in
14 the strain process, the H-charged samples did not undergo a work-hardening process during
15 the tensile test, with the relatively low fracture stress. The product of strength and elongation
16 decreases rapidly with the increase of hydrogen charging time and hydrogen concentration.

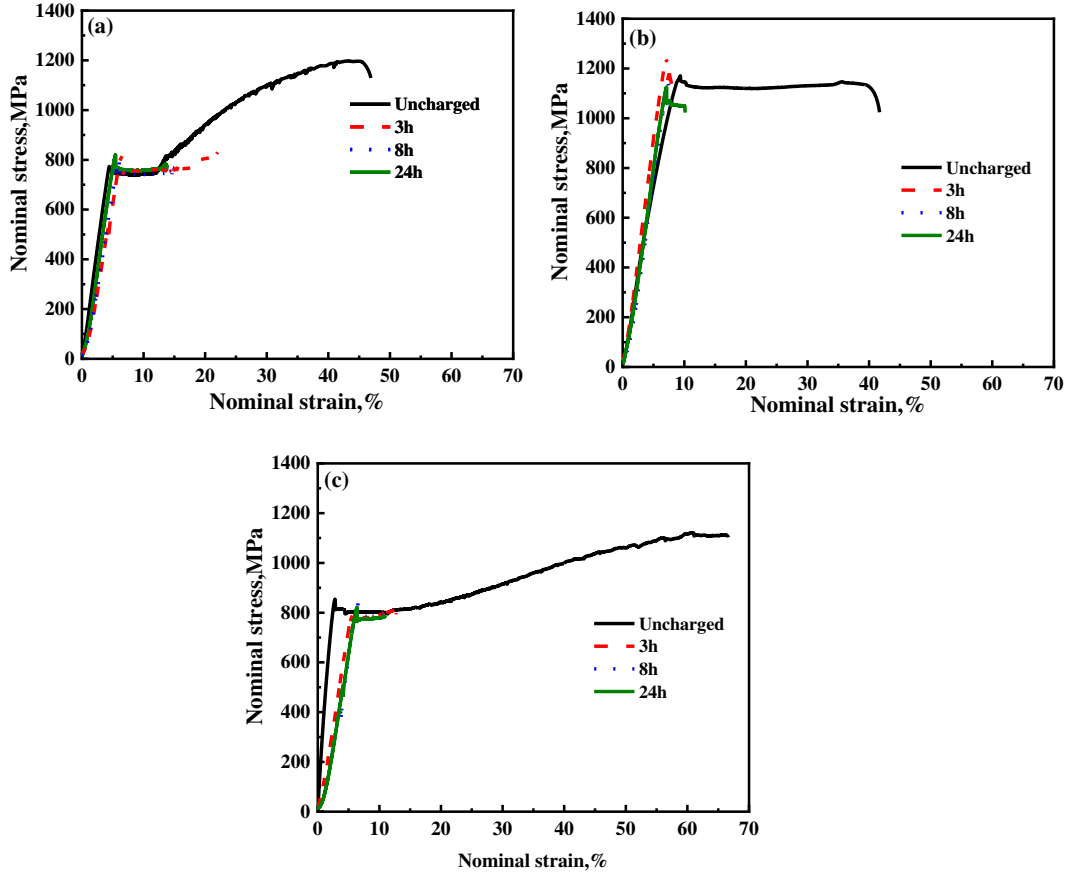


**Fig. 8 Stress-strain curves for MMSs under various pre-hydrogen charging SSRT
(a) M7B (b) M7C and (c) M10B**

The detailed data after SSRT was shown in Table 4, including fracture stress, the loss of ductility and hydrogen concentration. The loss of ductility, one kind of Embrittlement Index representing the sensitivity of HE, can be calculated by the following formula[39].

$$\varepsilon = l_0 - l'$$

$$\text{loss of ductility} = \frac{\varepsilon_0 - \varepsilon_H}{\varepsilon_0} \times 100\%$$

Where l_0 : the length of gauge part before SSRT; l' : the length of the gauge part after SSRT;
 ε : the ductility of the specimen; ε_0 : the ductility of the specimen in air; ε_H : the ductility of the specimen under hydrogen pre-charged condition;

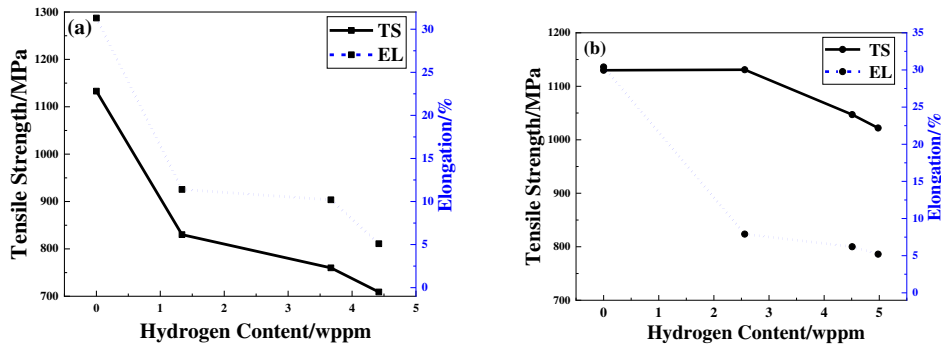
Fracture stress and elongation as a function of hydrogen content was plotted in Fig 9. Under

1 the same strain rate, fracture stress and ductility decrease gradually with the increase of
 2 hydrogen concentration. At the same hydrogen pre-charged condition, as shown in Fig 9,
 3 M7C always exhibits highest loss of ductility and the lowest loss of fracture stress among the
 4 MMSs. Compared with the hydrogen-uncharged samples, 3-hour hydrogen-charged samples
 5 saw a significant degradation of the elongation. So SEM fractographs of MMSs after 3-hour
 6 hydrogen pre-charging SSRT were observed as shown in Fig 10. The initiation of cracking
 7 and shear lip area of each specimen were observed at high magnifications, exhibiting a brittle
 8 fracture mode and secondary cracks observed at the same time. The HE mechanism of MMSs
 9 was explained by experimental results and fractograph observations below.

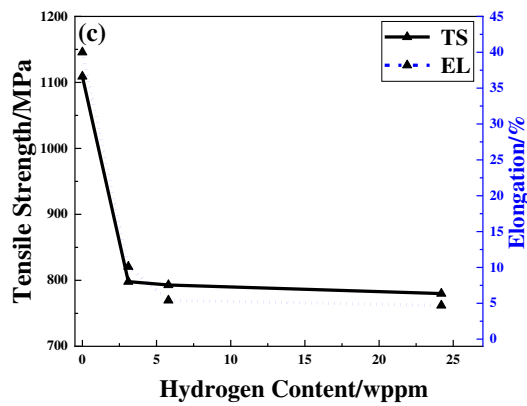
10 **Table 4 Mechanical properties and hydrogen content of the MMSs after SSRT under**
 11 **different pre-charged condition**

Steel	condition	Fracture stress/MPa	Ductility/%	Loss of ductility/%	The product of TS and ductility/GPa•%	Hydrogen content/wppm
M7B	No charged	1133	31.3	0	35.5	0.15
	Pre-charged 3 hours	830	11.4	60.9	8.8	1.34
	Pre-charged 8 hours	760	10.2	67.4	7.8	3.67
	Pre-charged 24 hours	709	5.1	83.7	3.6	4.42
M7C	No charged	1130	30.4	0	34.3	0.21
	Pre-charged 3 hours	1130	7.9	74.0	9.0	2.56
	Pre-charged 8 hours	1047	6.2	79.6	6.5	4.51
	Pre-charged 24 hours	1022	4.3	85.9	4.4	4.98
M10 B	No charged	1403	40.0	0	56.1	0.25
	Pre-charged 3 hours	798	12.7	68.3	10.1	3.1
	Pre-charged 8 hours	793	8.6	78.5	6.8	5.8
	Pre-charged 24 hours	780	5.9	85.3	4.7	24.2

1



2



3

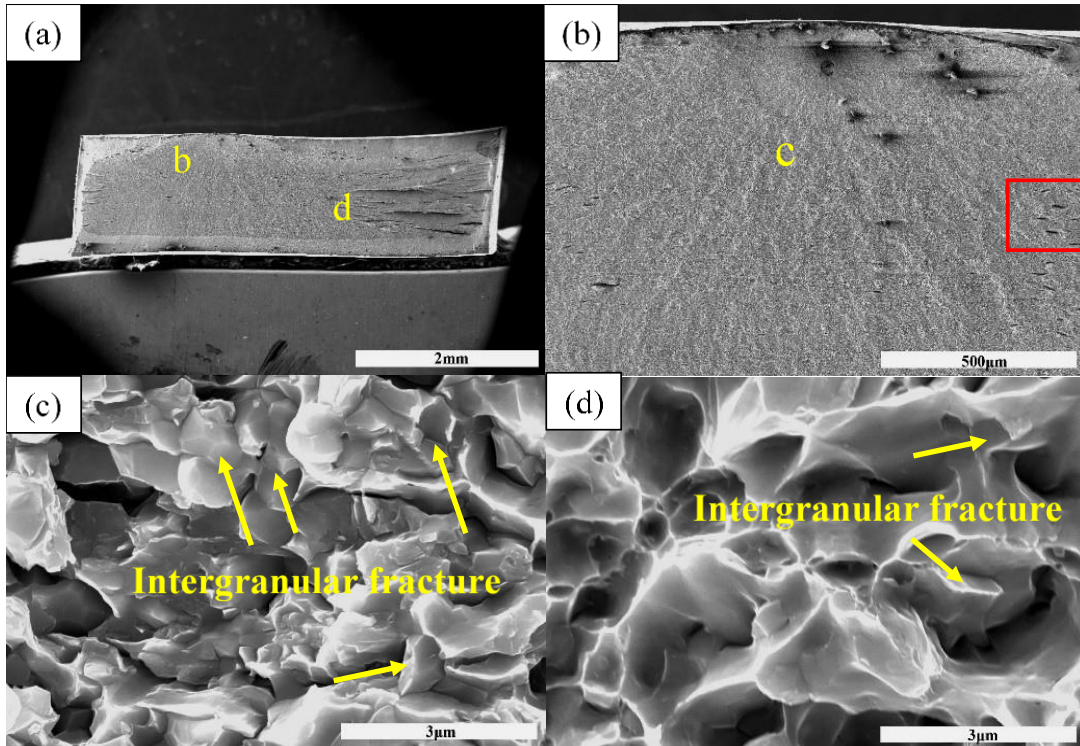
4 **Fig. 9 Tensile strength and elongation as a function of hydrogen content for (a)**
5 **M7B (b) M7C and (c) M10B**

6

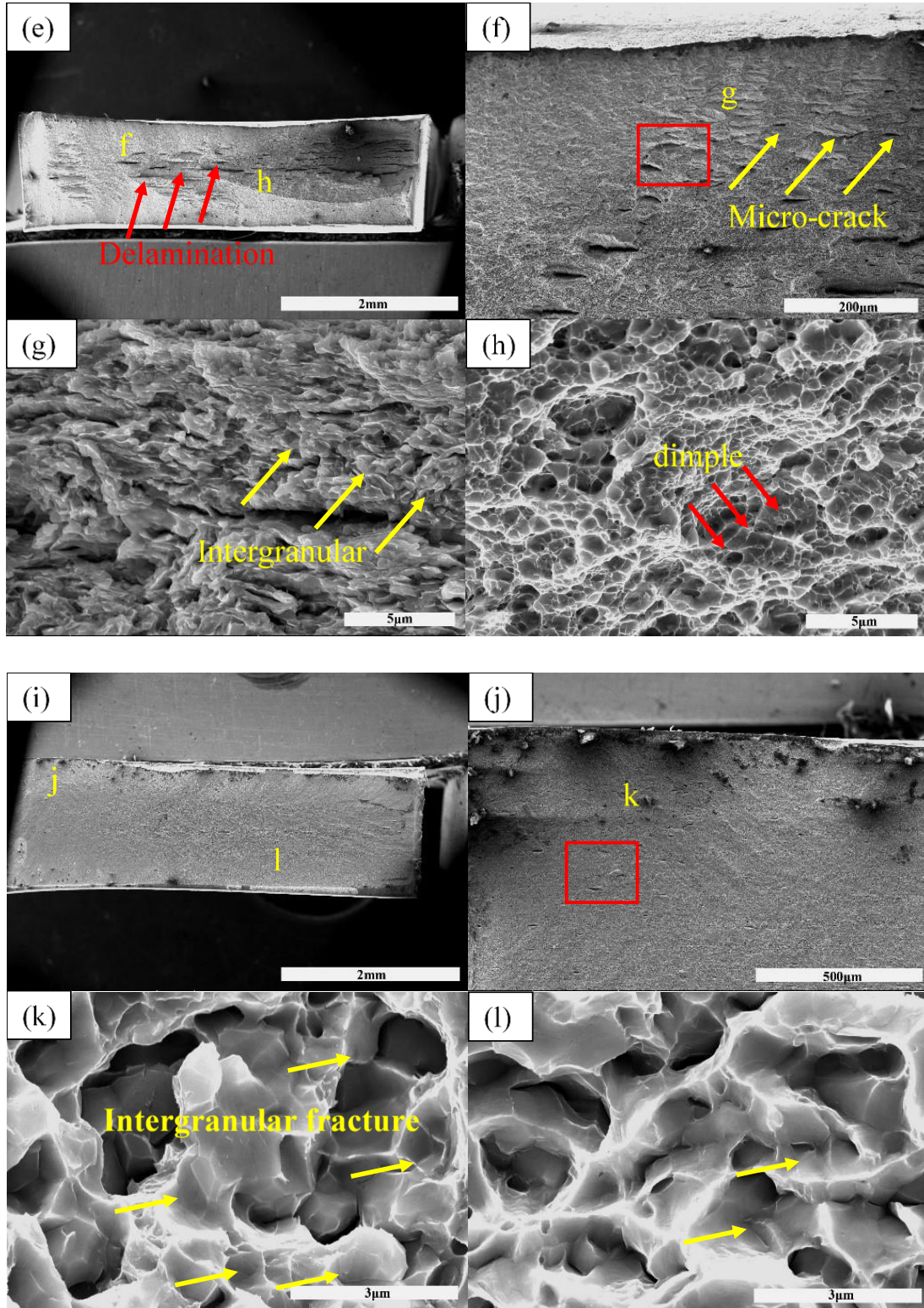
7 For M7B and M10B, after a lengthy batch-annealing process, the grain is uniformly fine
8 without defects and internal stress, ensuring the adequate diffusion of Mn and C. Due to the
9 entry of diffusible hydrogen, as shown in Fig.9 (a) and (c), the fracture stress and elongation
10 exhibited sharp drop at a certain hydrogen content. This certain content of hydrogen was
11 named ‘critical hydrogen concentration’, making the fracture transition from ductile
12 dominated fracture mode into brittle mode. The critical hydrogen concentration for M7B and
13 M10B, in this study, is 1.34 wppm and 3.10 wppm respectively. The samples after
14 hydrogen-charging shown different fracture surface compared with no hydrogen-charging
15 samples. Compared with Fig.4, fracture surface is smooth without delamination for M7B and
16 M10B in Fig.10 (a) and (i), while obvious delamination for M7C shown in Fig.10 (e). The
17 reason is that the occurrence of delamination is associated with the applied stress exceeding

1 yield strength. But for M7B and M10B, the fracture stress is not big enough to occur plastic
2 deformation degraded by the entry of more hydrogen. According to HEDE mechanism,
3 hydrogen atoms diffuse inwards and enrich at grain boundaries of austenite and decrease the
4 cohesive strength of material at crack tip to form continuous weak bond zone and
5 intergranular fracture occurs in M7B and M10B [16], shown in Fig.10 (c) (d) and (k) (l).
6
7 M7C shows different fracture mode from M7B and M10B due to different heat treatment and
8 hydrogen behaviour in material. The various fracture modes, for example, intergranular,
9 quasi-cleavage and dimple might be seen depending on the hydrogen concentration,
10 microstructure and stress intensity of crack tip [16]. The distributed lath-shaped austenite had
11 relatively low stability and it would deformed and transformed into martensite at lower strain
12 condition in M7C. As shown in Fig.3 and Fig.8, the stress of M7C reaches a higher level at
13 lower strain than that of M7B and M10B whether hydrogen-charging or not. Meanwhile, the
14 yield strength is close to tensile strength. The fracture stress of M7C did not decrease as
15 sharply as that of M7B and M10B after hydrogen-charging process, in Fig.9 (b). Under the
16 circumstances, stress has a dominated effect in fracture modes, consistent with discussion
17 about delamination occurring at stress concentration. It is generally acknowledged that the
18 delamination is the result of the coalescence of micro-cracks induced by stress. According to
19 red box Fig.10 (b) (f) (g), the amount of micro-cracks in M7C is much higher than that in
20 M7B and M10B. That explains that the delamination fracture appeared at half thickness of
21 cross-section in Fig.10 (e) and disappeared in Fig.10 (a) and (i). By fractography examination
22 of M7C after SSRT, shown in Fig.10 (h), it was concluded that the fracture showed the brittle
23 fracture mode at the edge of the specimen and ductile mode characterized with dimples in the
24 centre of the specimen. According to the adsorption-induced dislocation emission (AIDE) and
25 hydrogen assisted micro void coalescence (HDMC) mechanisms, the mixed fracture mode in
26 M7C after SSRT might be cause by the combination of hydrogen content and stress intensity
27 of crack tip. Firstly, hydrogen atoms are adsorbed at the region of stress concentration and
28 results in facilitating dislocation injection from a crack tip and then crack growth and
29 formation of microvoids by HELP. The micro-cracks initiation and propagation happened

1 after the joining of microvoids, as shown in Fig.10 (f). The micro-void coalescence dimple
2 produced due to the effect of hydrogen but they possess poor ductility. Final fracture occurs
3 due to shear stress so shear dimple presented, shown in Fig.10 (h). Brittle intergranular
4 fracture can be seen in Fig.10 (g) at the edge of the specimen due to the effect of hydrogen.
5



6



1

2

3 **Fig.10 Fracture surfaces of MMSs under 3-hour hydrogen pre-charging SSRT: (a)**
 4 **the whole fracture surface of M7B;(b) (d) magnified image of the part marked in (a); (c)**
 5 **magnified image of the part marked in (b);(e) the whole fracture surface of M7C;(f) (h)**
 6 **magnified image of the part marked in (e) and (g) magnified image of the part marked**
 7 **in (f);(i) the whole fracture surface of M10B;(j) (l) magnified image of the part marked**
 8 **in (i) and (k) magnified image of the part marked in (j);**

1 Retained austenite, as a strong hydrogen trap in MMSs, forces hydrogen to diffuse to the
2 boundary of ferrite and austenite or the interior of austenite. Austenite transforms into
3 martensite during plastic deformation induced by stress. The dissolved hydrogen in austenite
4 would diffuse into the stress concentration position of the matrix and promote the initiation of
5 a microcrack [34]. The fracture propagated quickly with the increase of stress. Observing the
6 fracture, it is found that some dimples filled with grains were generated by intergranular
7 cracking occurring along the boundaries of RA grains or the boundary of the dual phase. The
8 dissolved H in austenite diffuses to the interface during phase transformation, thus reducing
9 the cohesive bonding force between grains. Also, stress concentration at the crack leads to
10 intergranular cracking, which can be explained by the HEDE mechanism. The empty dimples
11 were generated by intragranular cracking occurring at grain boundaries. Hydrogen leads to
12 local deformation by facilitating dislocation emission, causing stress concentration in the
13 crack tip, showing the empty dimple in the fracture morphology.

14

15 **4. Conclusions**

16 In this paper, the effect of hydrogen concentration on the mechanical properties and fracture
17 behaviour and the interpretation of different HE mechanisms of medium Mn steels (M7B,
18 M7C, M10B) were studied through the hydrogen permeation test and slow strain rate tensile
19 test after hydrogen-charging. The conclusions drawn from this work include the following:

20 (1) Due to the different heat treatment conditions, the grain size of M7B and M10B is
21 relatively uniform, with a size of 1–3 μm , and the microstructure of M7C retains long
22 strip characteristics. The increase of Mn content increases the volume fraction of RA in
23 the specimen, resulting in a higher fraction of RA in M10B than in M7B and M7C. After
24 a short period of continuous annealing treatment, the stability of austenite in M7C is poor,
25 clearly changing at the beginning of strain. Therefore, the yield strength of M7C is much
26 higher than that of M7B, and there is no work-hardening stage on the stress-strain curve.
27 The RA in M7B and M10B is relatively stable and undergoes a continuous

1 work-hardening process after the yielding platform.

2 (2) Austenite content has a decisive influence on hydrogen diffusion rate. As the volume
3 fraction of austenite in M10B is two times that of M7B and M7C, austenite, as a block to
4 hydrogen diffusion, decreases the diffusion rate of hydrogen.

5 (3) If hydrogen content is more than the critical level of hydrogen which is known as critical
6 hydrogen concentration (H_c), then HE happened in material and seriousness of HE is
7 depend on the amount of hydrogen concentration. The H_c of M7B and M10B was
8 provided based on this study.

9 (4) The fracture morphology was determined by the combination effect of hydrogen content
10 and applied stress. For M7B and M10B, hydrogen plays a dominated role in determining
11 the brittle fracture after three-hour hydrogen-charging, while the fracture in M7C showed
12 the mixed fracture mode determined by the synergistic action of hydrogen content and
13 stress.

14 (5) The variety of mechanisms are available and responsible for HE of a material such as
15 HEDE, HELP, AIDE and HDMC. The HE in M7B and M10B can be explained by HEDE
16 mechanism. More than one mechanisms are responsible for degradation and
17 embrittlement of material. To reduce HE phenomena and interpret it clearly, selection of a
18 material is very much important. Even in the same material, the HE mechanism could be
19 different regarding to the region. The fracture surface of M7C showed mixed modes with
20 brittle edge and ductile centre. Still the actual mechanism which causes embrittlement
21 occurs in a material is unclear and research will be going on to identify the main
22 embrittlement causes of a material.

24 **Acknowledgement**

25 This work was supported by the National Natural Science Foundation of China [grant NO. U1660104].

1 **References**

- 2 [1] R.L. Miller, Ultrafine-grained microstructures and mechanical properties of alloy steels, *Metallurgical*
3 *Transactions* 3(4) (1972) 905-912.
- 4 [2] T. Furukawa, Dependence of strength–ductility characteristics on thermal history in lowcarbon, 5 wt-%Mn
5 steels, *Materials Science and Technology* 5(5) (1989) 465-470.
- 6 [3] L. Luo, W. Li, L. Wang, S. Zhou, X. Jin, Tensile behaviors and deformation mechanism of a medium
7 Mn-TRIP steel at different temperatures, *Materials Science and Engineering: A* 682 (2017) 698-703.
- 8 [4] P.J. Gibbs, E.D. Moor, M.J. Merwin, B. Clausen, J.G. Speer, D.K. Matlock, Austenite Stability Effects on
9 Tensile Behavior of Manganese-Enriched-Austenite Transformation-Induced Plasticity Steel, *Metallurgical &*
10 *Materials Transactions A* 42(12) (2011) 3691-3702.
- 11 [5] W.S. Dong, J.H. Ryu, S.J. Min, H.S. Yang, K. Lee, H.K.D.H. Bhadeshia, Medium-Alloy Manganese-Rich
12 Transformation-Induced Plasticity Steels, *Metallurgical & Materials Transactions A* 44(1) (2013) 286-293.
- 13 [6] H. Choi, S. Lee, J. Lee, F. Barlat, B.C. De Cooman, Characterization of fracture in medium Mn steel,
14 *Materials Science and Engineering: A* 687 (2017) 200-210.
- 15 [7] Z.C. Li, H. Ding, R.D.K. Misra, Z.H. Cai, H.X. Li, Microstructural evolution and deformation behavior in
16 the Fe-(6, 8.5)Mn-3Al-0.2C TRIP steels, *Materials Science & Engineering A* 672 (2016) 161-169.
- 17 [8] H. Huang, O. Matsumura, T. Furukawa, Retained austenite in low carbon, manganese steel after intercritical
18 heat treatment, *Metal Science Journal* 10(7) (1994) 621-626.
- 19 [9] H. Luo, J. Shi, C. Wang, W. Cao, X. Sun, H. Dong, Experimental and numerical analysis on formation of
20 stable austenite during the intercritical annealing of 5Mn steel, *Acta Materialia* 59(10) (2011) 4002-4014.
- 21 [10] W.Q. Cao, C. Wang, J. Shi, M.Q. Wang, W.J. Hui, H. Dong, Microstructure and mechanical properties of
22 Fe–0.2C–5Mn steel processed by ART-annealing, *Materials Science & Engineering A* 528(22) (2011)
23 6661-6666.
- 24 [11] J. Han, S.J. Lee, J.G. Jung, Y.K. Lee, The effects of the initial martensite microstructure on the
25 microstructure and tensile properties of intercritically annealed Fe–9Mn–0.05C steel, *Acta Materialia* 78(2)
26 (2014) 369-377.
- 27 [12] S. Thomas, N. Ott, R.F. Schaller, J.A. Yuwono, P. Volovitch, G. Sundararajan, N.V. Medhekar, K. Ogle, J.R.
28 Scully, N. Birbilis, The effect of absorbed hydrogen on the dissolution of steel, *Heliyon* 2(12) (2016) e00209.
- 29 [13] I.M. Robertson, P. Sofronis, A. Nagao, M. Martin, S. Wang, D. Gross, K. Nygren, Hydrogen embrittlement
30 understood, *Metallurgical and Materials Transactions A* 46(6) (2015) 2323-2341.
- 31 [14] R. Oriani, Whitney award lecture—1987: hydrogen—the versatile embrittler, *Corrosion* 43(7) (1987)
32 390-397.
- 33 [15] J. Venezuela, Q. Liu, M. Zhang, Q. Zhou, A. Atrens, A review of hydrogen embrittlement of martensitic
34 advanced high-strength steels, *Corrosion Reviews* 34(3) (2016) 153-186.
- 35 [16] S.K. Dwivedi, M. Vishwakarma, Hydrogen embrittlement in different materials: A review, *International*
36 *Journal of Hydrogen Energy* 43(46) (2018) 21603-21616.
- 37 [17] D.H. Herring, Hydrogen embrittlement, *Wire Forming Technology International* 13(4) (2010) 24-27.
- 38 [18] S.K. Dwivedi, M. Vishwakarma, Hydrogen embrittlement in different materials: A review, *International*
39 *Journal of Hydrogen Energy* (2018).
- 40 [19] Q. Liu, Q. Zhou, J. Venezuela, M. Zhang, A. Atrens, Hydrogen influence on some advanced high-strength
41 steels, *Corrosion Science* 125 (2017) 114-138.
- 42 [20] T. Depover, D. Pérez Escobar, E. Wallaert, Z. Zermout, K. Verbeken, Effect of hydrogen charging on the

1 mechanical properties of advanced high strength steels, *International Journal of Hydrogen Energy* 39(9) (2014)
2 4647-4656.

3 [21] J. Han, J.-H. Nam, Y.-K. Lee, The mechanism of hydrogen embrittlement in intercritically annealed
4 medium Mn TRIP steel, *Acta Materialia* 113 (2016) 1-10.

5 [22] B. Kan, Z.X. Yang, Z. Wang, J.X. Li, Q.J. Zhou, Y.J. Su, L.J. Qiao, A.A. Volinsky, Hydrogen redistribution
6 under stress-induced diffusion and corresponding fracture behaviour of a structural steel, *Materials Science and*
7 *Technology* 33(13) (2017) 1539-1547.

8 [23] J.P. Hirth, Effects of hydrogen on the properties of iron and steel, *Metallurgical Transactions A* 11(6) (1980)
9 861-890.

10 [24] M. Koyama, E. Akiyama, Y.-K. Lee, D. Raabe, K. Tsuzaki, Overview of hydrogen embrittlement in
11 high-Mn steels, *International Journal of Hydrogen Energy* 42(17) (2017) 12706-12723.

12 [25] H.K. Birnbaum, P. Sofronis, Hydrogen-enhanced localized plasticity—a mechanism for hydrogen-related
13 fracture, *Materials Science & Engineering A* 176(1-2) (1994) 191-202.

14 [26] A. Nagao, C.D. Smith, M. Dadfarnia, P. Sofronis, I.M. Robertson, The role of hydrogen in hydrogen
15 embrittlement fracture of lath martensitic steel, *Acta Materialia* 60(13) (2012) 5182-5189.

16 [27] S.P. Lynch, 2 - Hydrogen embrittlement (HE) phenomena and mechanisms, in: V.S. Raja, T. Shoji (Eds.),
17 *Stress Corrosion Cracking*, Woodhead Publishing 2011, pp. 90-130.

18 [28] M. Nagumo, T. Yagi, H. Saitoh, Deformation-induced defects controlling fracture toughness of steel
19 revealed by tritium desorption behaviors, *Acta Materialia* 48(4) (2000) 943-951.

20 [29] M. Nagumo, Hydrogen related failure of steels – a new aspect, *Materials Science and Technology* 20(8)
21 (2004) 940-950.

22 [30] M. Koyama, E. Akiyama, K.J.C.S. Tsuzaki, Effect of hydrogen content on the embrittlement in a Fe–Mn–C
23 twinning-induced plasticity steel, 59 (2012) 277-281.

24 [31] Y. Zhang, L. Wang, K.O. Findley, J.G. Speer, Influence of Temperature and Grain Size on Austenite
25 Stability in Medium Manganese Steels, *Metallurgical & Materials Transactions A* 48(5) (2017) 1-10.

26 [32] ASTM E8 / E8M-16a, Standard Test Methods for Tension Testing of Metallic Materials, ASTM
27 International, West Conshohocken, PA, 2016, www.astm.org.

28 [33] J. Andersons, M. König, Dependence of fracture toughness of composite laminates on interface ply
29 orientations and delamination growth direction, *Composites Science and Technology* 64(13) (2004) 2139-2152.

30 [34] S. Liu, X. Li, H. Guo, S. Yang, X. Wang, C. Shang, R.D.K. Misra, Selective role of bainitic lath boundary
31 in influencing slip systems and consequent deformation mechanisms and delamination in high-strength
32 low-alloy steel, *Philosophical Magazine* 98 (2018) 1-25.

33 [35] J. Tao, S. Hu, F. Yan, Y. Zhang, M. Langley, A study of the mechanism of delamination fracture in bainitic
34 magnetic yoke steel, *Materials & Design* 108 (2016) 429-439.

35 [36] J.H. Ryu, Y.S. Chun, C.S. Lee, H.K.D.H. Bhadeshia, D.W. Suh, Effect of deformation on hydrogen trapping
36 and effusion in TRIP-assisted steel, *Acta Materialia* 60(10) (2012) 4085-4092.

37 [37] T.K. Shan, S.H. Li, W.G. Zhang, Z.G. Xu, Prediction of martensitic transformation and deformation
38 behavior in the TRIP steel sheet forming, *Materials & Design* 29(9) (2008) 1810-1816.

39 [38] E. Owczarek, T. Zakroczymski, Hydrogen transport in a duplex stainless steel, *Acta Materialia* 48(12)
40 (2000) 3059-3070.

41 [39] F. Cusenza, S. Ringeval, S. Thiébaud, F. Buy, T. Paris, I. Moro, L. Briottet, V. Vignal, Study of the
42 Hydrogen Embrittlement Sensitivity of an X4CrNiMo 16.5.1 Stainless Steel and the Associated Electron Beam
43 Weld, ASME 2015 Pressure Vessels and Piping Conference, 2015.

44